

RSC Advances



This is an *Accepted Manuscript*, which has been through the Royal Society of Chemistry peer review process and has been accepted for publication.

Accepted Manuscripts are published online shortly after acceptance, before technical editing, formatting and proof reading. Using this free service, authors can make their results available to the community, in citable form, before we publish the edited article. This *Accepted Manuscript* will be replaced by the edited, formatted and paginated article as soon as this is available.

You can find more information about *Accepted Manuscripts* in the [Information for Authors](#).

Please note that technical editing may introduce minor changes to the text and/or graphics, which may alter content. The journal's standard [Terms & Conditions](#) and the [Ethical guidelines](#) still apply. In no event shall the Royal Society of Chemistry be held responsible for any errors or omissions in this *Accepted Manuscript* or any consequences arising from the use of any information it contains.



Fabricating three-dimensional mesoporous carbon network-coated LiFePO₄/Fe nanospheres using thermal conversion of alginate-biomass

Hui Guo, Xudong Zhang*, Wen He*, Xuena Yang, Qinze Liu, Mei Li and Jichao Wang

Received 00th January 20xx,
Accepted 00th January 20xx

DOI: 10.1039/x0xx00000x

www.rsc.org/

Lack of cathode materials with high energy density has become the bottleneck for the development of low-cost lithium-ion batteries (LIBs). Here, we develop three-dimensional mesoporous carbon network (3DMCN)-coated LiFePO₄/Fe nanospheres (3DMCN-LFP/Fe-NSS) for tackling this problem. This new nanocomposite cathode is synthesized by using thermal conversion of natural alginate (ALG)-biomass. In the heat-treated process, ALG hydrogel with "egg-box" structure was transformed into unique 3DMCN, while some of iron ions were reduced to iron metal. The 3DMCN and Fe metal coating not only reduces the anisotropy and grain size of LiFePO₄, but also enhances its electron conductivity and lithium-ion diffusion coefficient. This makes this specially designed nanocomposite give a remarkable synergy effect for both lithium storage and transfer kinetics. After 256 cycles the discharge capacity (173 mA h g⁻¹) was still higher than the theoretical capacity of LiFePO₄ and its capacity retention rate is 99%. Even at a high current rate of 10 C, the discharge energy density is still 6.2 times that of commercial LiFePO₄. More importantly, this nanocomposite is created through a simple and cost-effective approach. This work also opens a new vista for applying renewable biomass conversion technology to develop superior LIBs.

1. Introduction

Despite the development of various new cathode materials, LiFePO₄ cathode materials are still the most widely research for the LIBs,¹⁻³ owing to its simple preparation and excellent electrochemical performances, such as long cycle life, thermal stability (Oxidation temperature >350 °C), high theoretical capacity (170 mA h g⁻¹), stable lithium-ion insertion/extraction reactions (3.5 V vs. Li⁺/Li) and phase transformations.²⁻⁴ However, the sluggish Lithium-ion diffusion (10⁻¹⁶–10⁻¹⁴ S cm⁻¹) across the LiFePO₄/FePO₄ interface and low electrical conductivity (1.8×10⁻⁹ S cm⁻¹) still need to be further improved. To enhance the performances of LiFePO₄ material, two main strategies have been adopted by reducing the active particle size, coating conductive layer on the LiFePO₄ particles with carbon, metals or conductive polymer.⁵⁻¹¹ Recently, the Iron (Fe) metal-based nanoparticles, such as Fe/Fe₃C, Fe/Fe₃O₄, Fe/Ni alloys and Fe/Si alloys have attracted intensive attention for their possible applications in LIBs anode materials,¹²⁻¹⁶ but little is known about the applications in LIBs cathode materials. The Fe metal-based materials offer several advantages with respect to other metal-based materials because of their flexible synthetic routes, good electrical conductivity and ductility, and comparatively

inexpensive precursor materials. Even though Fe metal is almost inactive for Lithium-ion intercalation, the authors pointed out that Fe atoms can provide lots of free electrons and act as a conductive agent, which can improve the electrochemical performance of the LiFePO₄ cathodes (Figure 5a).^{13, 17, 18} Besides, α-Fe crystals have a simple cube accumulation with high porosity of 48 %, which can significantly increase the permeability of the electrolyte and thus facilitate lithium-ion diffusion.

Under the guidance of current strategies to remove lithium-ion and electronic transport limitations in LiFePO₄ structure, carbon-coated has been considered as a efficient, facile, and feasible process.¹⁹⁻²² Due to the intrinsic electrical conductivity, the carbon framework not only increased electron migration rate, but also controlled the crystal growth of LiFePO₄. The nanoparticles can effectively shorten the distance of lithium-ion diffusion. The carbon framework coated on the surface of LiFePO₄ nanoparticles was used as a reducing agent in the synthesis, and can also buffer volume change of LiFePO₄/FePO₄ phase transformations during cycles.²³ Carbon coating usually derived from organics pyrolysis by organic precursor method or simple substance carbon (e.g. graphene) directly added.²⁴⁻³⁰ Among the different carbon materials, biocarbon materials have become the key of nanobiotechnology to creating extraordinary inorganic structures and morphologies due to its simple and efficient characters and unique nanostructures.³¹⁻³³

Institute of Materials Science and Engineering, Qilu University of Technology, Jinan 250353, China. Tel: +86 531 89631080; Fax: +86 531 89631518; *Corresponding author. *E-mail: zxd1080@126.com ; hewen1960@126.com.

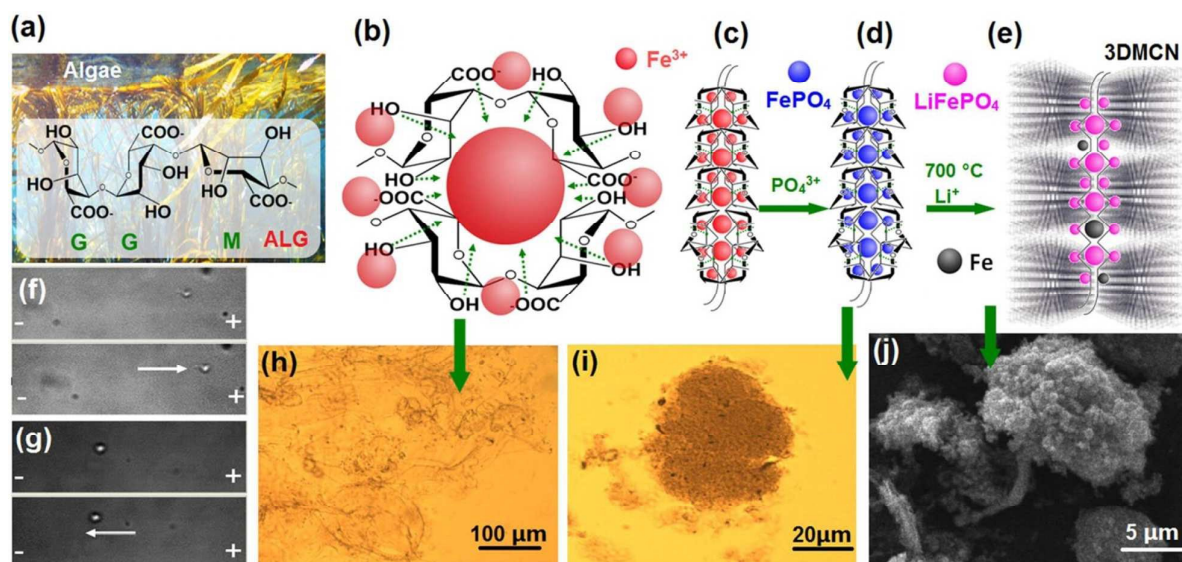


Figure 1 Formation mechanism of the 3DMCN-LFP/Fe-NSs. (a) the chemical structure of ALG and photo of natural algae. (b-d) Schematic illustrations of the synthesis route for the ALG-FePO₄ hydrogel: (b) self-assembly of the ALG biomolecules with Fe³⁺, (c) "egg-box" structure of ALG-Fe hydrogel, (d) FePO₄/ALG hydrogel. (e) Schematic drawing of 3DMCN-LFP/Fe-NSs. (f and g) Micro electrophoresis images of ALG-hydrogel particles (f) and ALG-Fe hydrogel particles (g) at optimum conditions (PH=6, 27.2 °C). (h and i) Polarized-light micrograph images of ALG-Fe hydrogel particles (h) and FePO₄/ALG precursor (i). (j) SEM image of 3DMCN-LFP/Fe-NSs following calcination.

Many diverse biomaterials with hierarchical structures have been used as biotemplates to synthesize various novel functional materials.^{34, 35} Hydrophilic polysaccharides is a promising type of the renewable biomass carbon resources, and its features are abundant in natural resources, biodegradable and antiviral.³⁶ Alginates (ALG) is a natural linear polysaccharide purified from phaeophyceae and contains a large amount of carboxylic and hydroxy groups.³⁷⁻⁴⁰ In ALG structure the β -D-mannuronic (M) and α -L-guluronic (G) acid units (Figure 1a) random arrangement. The carboxylic groups of the G residues exhibited better metal ions chelation activity can form a typical hydrogel structure with "egg-box" model. Although ALG have been applied as binders for LIBs,^{39, 41} relatively few reports of ALG are directly involved in synthesis process of electroactive materials. In this paper, we attempted to design and fabricate the LiFePO₄/Fe nanospheres (LFP/Fe-NSs) coated with 3DMCN via a facile and green method. In synthesis the ALG are used as the structural template of 3DMCN. The results indicate that the "egg-box" structure of 3DMCN could control crystal size to the LiFePO₄/Fe nanospheres, and also provide conductive network for the electron delivery, which enhances high rate performance and cycle stability. A suitable amount of Fe metal crystal particles formed on the surface of LiFePO₄ can significantly improve its electrical conductivity. This work is instructive for fabrication and design of nanostructured electrodes with extraordinary properties from biomass renewable resources.

2. Experimental

2.1 Synthesis of 3DMCN-LFP/Fe-NSs

The 3DMCN-LFP/Fe-NSs composite was prepared via a green route with ALG as biotemplate. First, 20 ml 0.5M Fe(NO₃)₃ solution was added to the purified ALG-hydrosol with stirring at 90 °C

(expressed as 3DMCN-LFP/Fe-NSs) and 30 °C (expressed as LFP/Fe) for 60 min. The high water-bath temperature is to reduce viscosity and improve the activity of polymer chain. Then, 0.01 mol (NH₄)₂HPO₄ and aqueous solution were added to the ALG-Fe hydrogel with stirring for 12h to form a uniform beige precipitation in the system at room temperature with pH balance of 4. In order to protect the porous structure of carbon aerogel, replacement of water by ethanol, and the deposit was dried in oven at 60 °C. Finally, the dry FePO₄/ALG mixtures were mixed with 0.01 mol LiOH•H₂O and 0.0015 mol glucosum anhydricum. The mixture was heated in nitrogen atmosphere at 700 °C for 8 h. For comparison, LFP/C (common carbon-coated under the same conditions) and the commercial LiFePO₄ sample (LFP) were applied. The operation principles and processes were described in detail within Supplementary Figure S1.

2.2 Materials characterization

First of all, to identify the crystal phases composition of the synthesized samples, X-ray diffraction (XRD) employing with Cu-K α radiation (LabX XRD-6100; Shimadzu) was used. And then, the structure of molecules and biocarbon was further tested and analyzed. FT-IR measurements were performed using a Nicolet Nexus spectrometer (Nicolet, NEXUS 470, USA) by using a KBr wafer technique. Raman spectrum were collected on a LabRAM HR800 (HORIBA, France) with a He-Ne laser (excitation line 633 nm) as the excitation source. All reported spectra underwent baseline correction. Meanwhile, electrical microscope analysis brings us a direct view of the morphology, porous structure, and crystal structures of the synthesized samples. Scanning electron microscopy (SEM) images of the samples were obtained using a FEI Quanta 200 environmental scanning electron microscope equipped for surface morphological studies. High-resolution

transmission electron microscopy (HRTEM) images were obtained using a Philips Tecnai 20U-TWIN microscope, working at 300 kV. To further investigate of pore structure, the nitrogen (N_2) adsorption-desorption isotherms and pore size distributions were carried out at -196°C using a surface area and porosity analyzer (Micromeritics, Gemini V2380, USA).

2.3 Electrochemical evaluation

The electrochemical tests were evaluated using LIR2032 coin-type cells. The half-cell were assembled by using lithium metal as a active anode and polypropylene membrane as a separator and the working electrode as the cathode in high purity argon filled inert glove box. To prepare working electrodes, a mixture of the LiFePO_4 sample with acetylene black and polyvinylidene fluoride were uniformly dispersed (8:1:1 wt%) in N-methyl pyrrolidone to prepare the slurry. The slurry was coated over a aluminum-foil. The electrolyte consist of 1 M LiPF_6 solution in ethylene methyl carbonate/ethylene carbonate/dimethyl carbonate mixture (1:1:1 vol%). The charge/discharge tests of LiFePO_4 cathode material were evaluated on Channels battery analyzer (CT3008W) at different rates over the potential range between 2.0 and 4.2 V cut-off voltage. The electrochemical impedance (EIS) and Cyclic voltammetry (CV) measurements were performed on a PARSTAT 2263 electrochemical workstation. All the process were performed at 25°C .

3. Results and discussion

3.1 Forming mechanism analysis of 3DMCN-LFP/Fe-NSs

ALG-enhanced electrochemical performances of the 3DMCN-LFP/Fe-NSs nanocomposites were able to identify for the first time. ALG is a sort of hydrophilic gels with strong hydration and excellent stability at pH 4 to 10.³⁷ Moreover, lots of hydrophilic anion groups ($-\text{OH}$, $-\text{COO}^-$) on the ALG surface (Figure 1a) not only can directly to promote interaction with Fe cations by electrostatic interaction (Figure 1b),^{40,42,43} and can be chelated into several chains to form a "box" structure with Fe^{3+} (Figure 1c). After the FeNO_3 precursor react with ALG, most of the Fe^{3+} were caught into the "box" structure of polymer chain. With CH_3COONa and $(\text{NH}_4)_2\text{HPO}_4$ aqueous solution was added into the ALG-Fe hydrogel, CHCOO^- could improve HPO_3^{2-} ionization, the PO_4^{3-} combined with Fe^{3+} and the active FePO_4 in situ precipitated in the "box" structure providing a widespread nucleation sites (Figure 1d).

The adsorption interactions of the ALG with Fe^{3+} were demonstrated by using JS94H micro-electrophoresis and Meiji ML9420 binocular polarizing microscopy. Figure 1f shows that the ALG-hydrogel particles dissolved in anhydrous ethanol move towards the anode and its zeta potential is -29.9 , indicating that ALG was negatively charged. When ALG adsorb Fe^{3+} after heat treatment at 90°C , the surface of ALG was positively charged as shown in Figure 1g and its zeta potential is 3.25 . The two electrophoresis images demonstrate the interaction of the ALG surface with the Fe^{3+} from the charge change of the particle surface. Polarized-light microscopy (PLM) images show the transparent yellow ALG-Fe hydrogel (Figure 1h) and a FePO_4/ALG precursor particle formed by the accumulation of dense tiny particles (Figure 1i), respectively. The SEM image of the 3DMCN-LFP/Fe-NSs

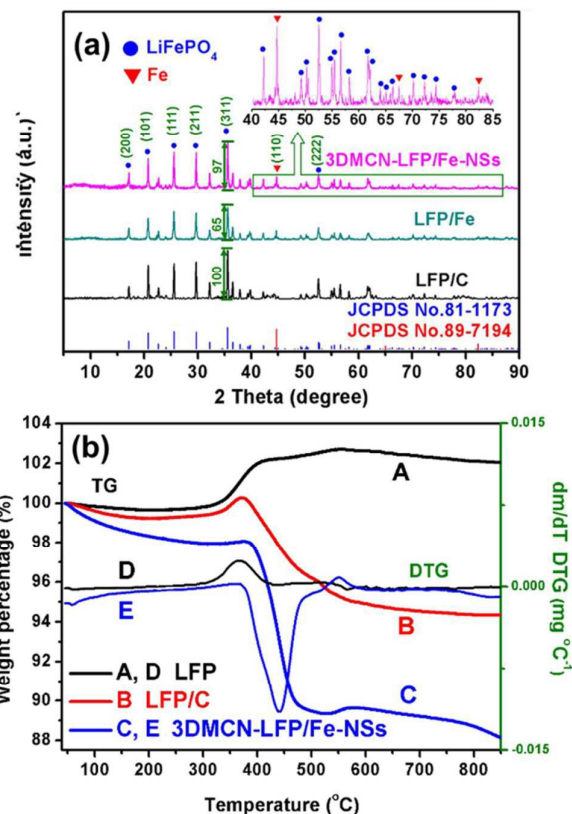


Figure 2 Phase characterization (a) XRD patterns of the samples synthesized under different conditions. (b) The thermogravimetric (TG) curves of the 3DMCN-LFP/Fe-NSs, LFP and LFP/C samples tested in air environment and the derivative thermogravimetric (DTG) analysis of the 3DMCN-LFP/Fe-NSs and LFP.

sample (Figure 1j), displaying the large particles with honeycomb structure from gel structure of FePO_4/ALG precursor.

As stated above, a possible formation mechanism of FePO_4 precursor is proposed in Figures. 1cd. Then by means of an in-situ composite carbonization and crystallization heat treatment in a reducing atmosphere, 3DMCN-LFP/Fe-NSs are synthesized (Figure 1e). During pyrolytic degradation, the gel network framework structure of ALG is decomposed to form 3DMCN. In the meantime, it also provided the carbon-rich conditions, which further facilitated the reduction of iron cation to Fe metal. 3DMCN can significantly increase the permeability of the electrolyte and thus facilitate diffusion of lithium-ion and also effectively restrict the growth of the LiFePO_4 nanoparticles. Fe metal is known as a conducting metal with the resistivity of $97.8\text{ n}\Omega\text{-m}$, which moves electric charges around easily. The pure biocarbon powders gained by carbonizing ALG have conductivity of $1.9 \times 10^{-4}\text{ S cm}^{-1}$, which measured by the RTS-8 four-probe conductivity meter. Therefore, the conducting synergy between the 3DMCN and Fe metal particles could improved significantly the conducting property of LiFePO_4 nanospheres. In the synthetic process, the chemical bond linkages between ALG biomolecules with iron cation and the in situ nanocomposite linkages between LiFePO_4 nanoparticles with the 3DMCN were studied by FT-IR for further analysis (Supplementary Figure S2). Through the FT-IR spectroscopy results, we have

verified that the deposition and self-assembly mechanism shown in Figure 1 is feasible for synthesizing 3DMCN-LFP/Fe-NSs.

3.2 Structure characterizations and analysis

The XRD results of Figure 2a indicate that the main crystal structure of all the samples have orthorhombic olivine-type structure of pure phase LiFePO_4 (JCPDS No.81-1173) with the space group Pnmb ,⁴⁴ and the sharp diffraction peaks indicate that the sample is well crystallized.⁴⁵ By contrasting the three samples XRD patterns, it can be seen that the 3DMCN-LFP/Fe-NSs and LFP/Fe composite synthesized by adding ALG hydrosol have the diffraction peaks matched with Fe metal (JCPDS No.89-7194) at 44.8, 65 and 82 degrees.⁴⁶ Combined with the test result of carbon content (Supplementary Table S1e), the Fe metal content in 3DMCN-LFP/Fe-NSs sample is about 3.1 wt%, and that of LFP/Fe sample is 2.7%, calculated by using Jade 6 XRD pattern-processing software, which indicates that a small amount of iron cation were reduced into Fe metal. The result can also be proven by TG analysis (Figure 2b). In the TG curve of the commercial LFP sample (Figure 2bA), about 2.5 % weight gain was observed in the temperature range of 350–550 °C, completely attributing to the oxidation course of Fe^{2+} in LiFePO_4 . Figure 2bB shows the weight loss process of carbon oxidation and decomposition.^{45, 47} The TG curve of 3DMCN-LFP/Fe-NSs (Figure 2bC) also has a weakly weight increase stage in the temperature range of 530–600 °C, which is mainly attributed

to the oxidation courses of Fe metal and residual Fe^{2+} . The total Fe metal content computed by the TG curve was about 1.23% (Supplementary equation S4), this result is lower than the result of XRD, which can be explained by the residual carbon decomposition (Figure 2bB). Figures 2bDE show the DTG curves of LFP and 3DMCN-LFP/Fe-NSs samples. The DTG curve of 3DMCN-LFP/Fe-NSs more clearly illustrates the stage in the temperature range of 530–600 °C, and the stage did not appear in LFP/C sample.

Besides, no obvious characteristic peaks of crystalline carbon retrieved in the diffraction patterns of the samples, indicating that the residual carbon derived from ALG pyrolysis has an amorphous structure.^{4, 45} This result is consistent with the the result of HRTEM and Raman spectrum analysis. In addition, the diffraction peaks of LiFePO_4 in 3DMCN-LFP/Fe-NSs sample are stronger than that of LFP/Fe samples, implying the effect of water bath temperature on the crystallinity. The summary of the structural features and performances for the samples synthesized at different conditions are given in Supplementary Table S1a–f.

HRTEM is an important means of crystal structure determination on the atomic scale.²³ Here, it can also be combined with others test to further intuitive analysis the effect of ALG biotemplates on the structure. The HRTEM images of the 3DMCN-LFP/Fe-NSs sample with different resolution are exhibited in Figure 3. Natural biomass tend to form porous structure.²²

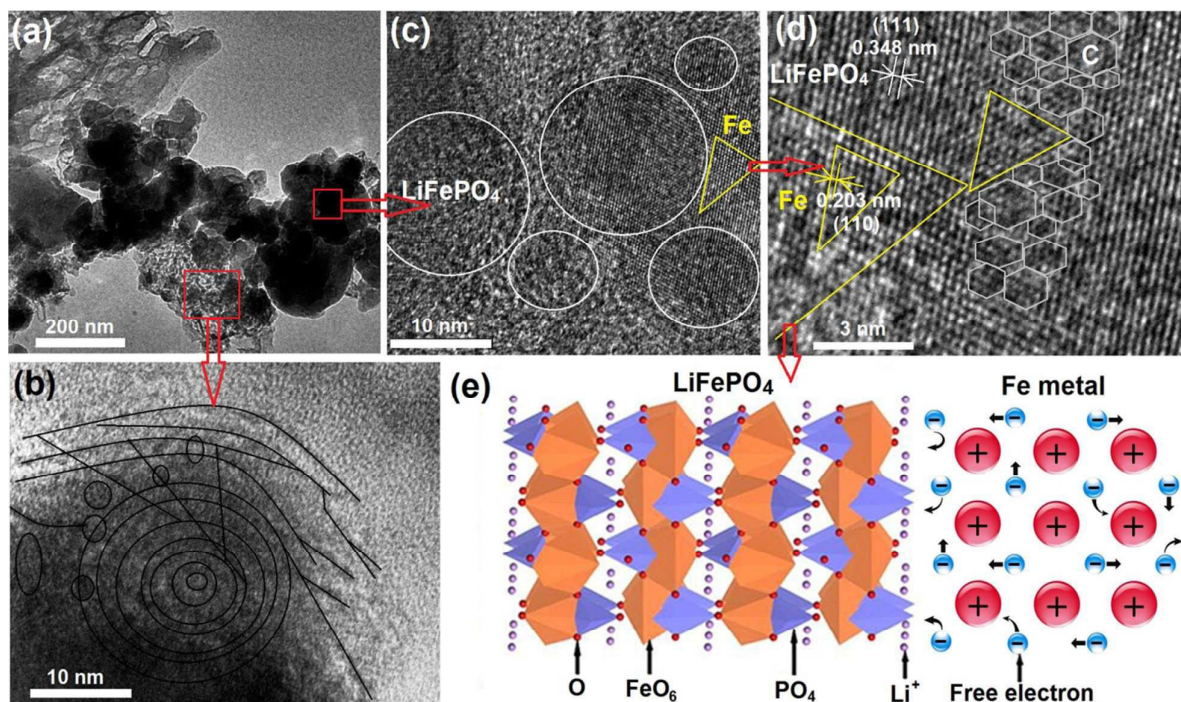


Figure 3 HRTEM images of 3DMCN-LFP/Fe-NSs sample. (a) Low magnification image showing an overview. (b) An enlarged image in (a), showing the network structure of 3DMCN. (c) An enlarged image in (a), showing a nanocomposite structure in which LiFePO_4 nanospheres and triangle Fe metal nanoparticles were dispersed in 3DMCN. (d) An enlarged image in (c), showing the lattice images of LiFePO_4 and Fe metal, and the nanostructure of biocarbon in 3DMCN. (e) Structure models of LiFePO_4 and Fe metal, showing that the free electrons in Fe metal can improve the lithium-ion diffusion performance of LiFePO_4 .

Figure 3a is a low magnification image of the microscopic structure, displaying the dark spherical particles with size (50–200 nm) and 3DMCN structure with a hierarchical pore structure. This was consistent with the results observed in SEM (Figure 1j) and the pore-size-distribution tests (Supplementary Figures S4cd). An enlarged image in Figure 3b shows more clearly the nanoscale network structure of 3DMCN. Figure 3c intuitively shows that a sphere-like particle in Figure 3a was composed of smaller LiFePO_4 nanospheres and triangle Fe metal nanoparticles dispersed in 3DMCN, in which they accumulated together compactly.

As shown in Figure 3d, the biocarbon particles in 3DMCN have no obvious lattice fringes,^{6, 48} indicating the biocarbon in sample was a typical amorphous state, which is consistent with the Raman test (Supplementary Figure 4a). Disordered carbon possesses vast defects and weak the anisotropy of the surface properties can provide additional active sites for lithium-ion storage and electron conduction, can also relax strain stress for volume change in the charge/discharge and crystal growth process.⁴⁹ Figure 3d shows more clearly that the lattice fringe spacing of (111) for LiFePO_4 is 0.348 nm and a triangle Fe metal nanoparticle with the (110) lattice fringe spacing of 0.203 nm was formed on the surface of LiFePO_4 particle in situ. Schematic models of LiFePO_4 and Fe metal in Figure 3e show that the free electrons in Fe metal can improve the lithium-ion diffusion performance of LiFePO_4 . The experiment results further show that the precipitation reactions of crystal particles occurred in the self-assemble structure of ALG biomolecules. The "box" structure of 3DMCN can provide

nucleation site and inhibit the abnormal grain growth of $\text{LiFePO}_4/\text{Fe}$ nanoparticles in the preparation process. 3DMCN also improves its electronic conductivity and offers effective buffering to maintain the composite cathode structure in charging and discharging process.

3.3 Electrochemical properties

The electrochemical performances of the synthesized samples used as a cathode in a half-cell were examined and compared by constant current charge-discharge (CD) tests in the first place. The typical first charge-discharge curves and capacity retention of 3DMCN-LFP/Fe-NSs, LFP/Fe, LFP/C, and pure LFP at a current rate of 0.1 and 0.5 C are shown in Figure 4a and 4b. In comparison with LFP blank sample and all synthesized samples with different preparative conditions, the average specific capacity of the first discharge for 3DMCN-LFP/Fe-NSs sample is $177.3 \text{ mA h g}^{-1}$, which is higher than the others. The 3DMCN-LFP/Fe-NSs sample has longer initial charge-discharge curves with a longer platform, higher capacity retention at 0.5 C and lower electrochemical polarization, which indicate the shorter and steady 1D transport of lithium-ion.¹⁹ In order to get the optimum reaction conditions, the effects of the different water-bath temperature and time on the electrochemical performance is shown in Supplementary Figure S5. Simply, the best water-bath temperature and water-bath time for 3DMCN-LFP/Fe-NSs sample are 90°C (Figure S5a) and 60 min (Figure S5b), respectively.

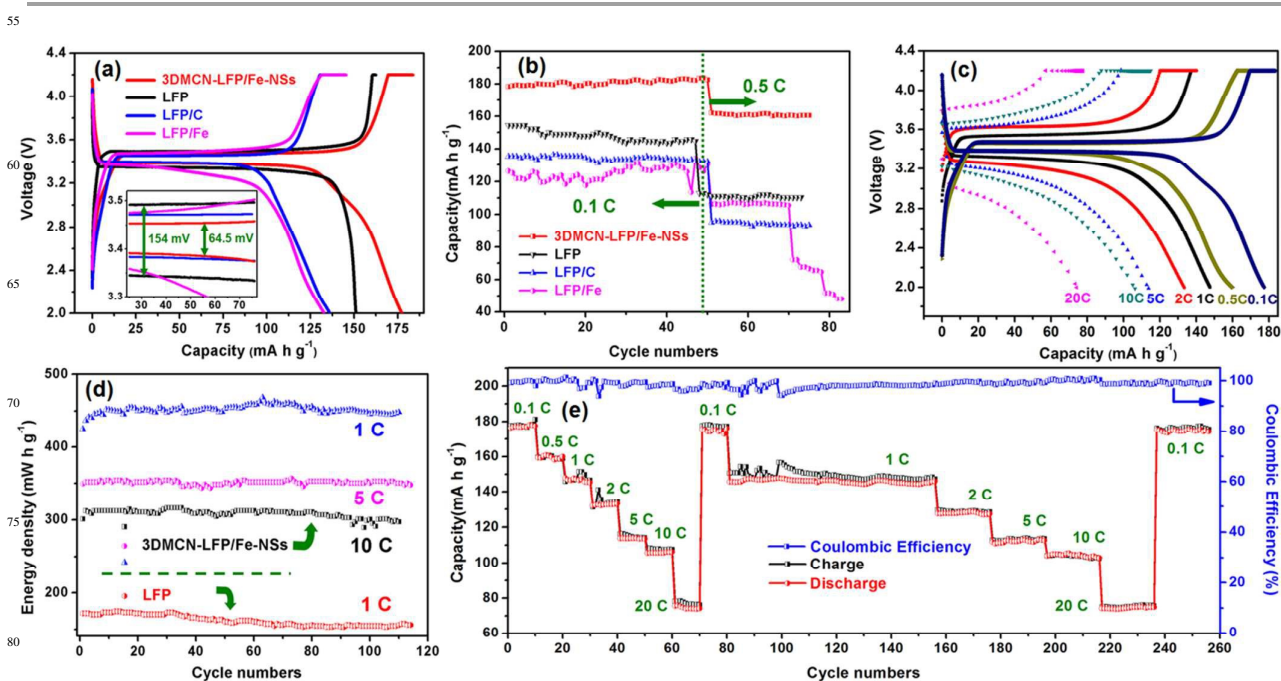


Figure 4 Electrochemical properties of the different cathodes for the coin cells tested between 2.0 and 4.2 V. All the process were performed at 25°C . (a) First charge-discharge curves of the different cathodes at 0.1 C. The inset is the embedded potential interval between the charge-discharge operating flat voltage. (b) Discharge capacity retention of the different cathodes at different rates. (c) First charge-discharge curves of 3DMCN-LFP/Fe-NSs cathode at different rates: 0.1 C, 0.5 C, 1 C, 2 C, 5 C, 10 C and 20 C. (d) Comparison of the discharge specific energy of 3DMCN-LFP/Fe-NSs and LFP cathodes at different current rates. (e) Capacity retention and coulombic efficiency of 3DMCN-LFP/Fe-NSs cathode for 256 cycles at different rates.

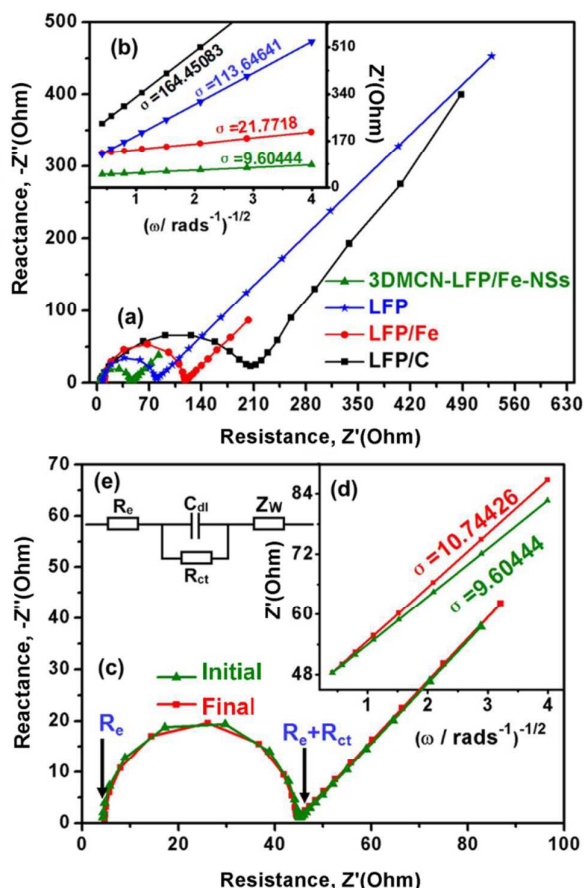


Figure 5 Electrochemical impedance spectroscopy studies. (a) Nyquist plots of the different cathodes vs. lithium metal anode to derive lithium-ion chemical diffusion coefficient at room temperature. (b) The plots of impedance as a function of the inverse square root of angular frequency in the Warburg region in (a). (c) Initial and final cycles of the Nyquist plots at 5C. (d) The plots of impedance as a function of the inverse square root of angular frequency in the Warburg region in (c). (e) The inset is an equivalent circuit model (R(CR)W) for the analysis of the impedance spectra.

10

Figure 4e shows the cyclability of 3DMCN-LFP/Fe-NSs sample cell at 0.1 C, 0.5 C, 1 C, 2 C, 5 C, 10 C and 20 C cycled 10 times each. After 70 cycles at different rates with a deep cycle (2.0 V-4.2 V),^{5, 50} the cell still delivered a discharge capacity of 175.7 mA h g⁻¹ and retained 99 % of its initial capacity at the 0.1 C rate. Moreover, a reversible capacity of 145.9 mA h g⁻¹ and 105.3 mA h g⁻¹ were still recoverable and sustainable after another cycles with small losses at the 1 C and 10 C rate, confirming structural stability. The results are comparable to that of Zhang et al. at high rate.⁶ Although the specific capacity gradually decreases with increasing current rate (Figure 4c),⁵¹ a high coulombic efficiency close to 100% has been achieved at different rates. Even at the high current rate of 20 C, the cell also maintained high coulombic efficiency. Here we tried the new rule in testing, and the related results show that the nanocomposites have better stability after dramatic changes (at the 80 to 100th cycles) from 0.1 to 1 C. Figure 4d show that the 3DMCN-LFP/Fe-NSs cathode is able to reach much higher energy

densities at higher discharge current rates than those of LFP sample. The most impressive discharge capacity of 3DMCN-LFP/Fe-NSs sample is very stable in the process of cycles, this could be attributed to the unique honeycomb structure of 3DMCN, the excellent morphology and dense packing of LFP/Fe-NSs, and the existence of Fe metal. This causes a significant increase in rate capability and coulombic efficiency.

3.4 Lithium-ion diffusion coefficient

Electrochemical impedance and Lithium-ion diffusion are the important factors affecting electrochemical performance.⁵² To further understand the electrode kinetics of the different samples, EIS and CV methods were carried out. Figure 5a shows the typical Nyquist plots of samples synthesized, each EIS curves has a starting point in the Z' axis, approximate semicircle and oblique line (Supplementary Figure S6).

The modified equivalent circuit shown in Figure 5e was used to model this impedance behavior.⁵³ The first step is to get the linear fitting of Z' vs. $\omega^{-1/2}$ (Figure 5b and Supplementary equation S6), and then get the slope (σ). Finally, substituting σ value into the coefficient equation (Supplementary equation S5), the coefficients of lithium-ion diffusion can be easily obtained. The results show that the lithium-ion diffusion coefficient (D_{Li}) values of the 3DMCN-LFP/Fe-NSs, LFP/Fe, LFP/C and LFP samples are 2.37×10^{-13} , 4.60×10^{-14} , 8.07×10^{-16} , and 1.68×10^{-15} cm² s⁻¹, respectively. Exciting results indicate that the 3DMCN-LFP/Fe-NSs cathode has a better D_{Li} value and the smallest charge-transfer impedance (Z_{Rct}) value (41 Ω).⁵⁴ The smallest Z_{Rct} value suggests that the high electrical conductivity of 3DMCN and appropriate amount of Fe metal for electron transfer, resulting in the higher energy density (Figure 4d). Meanwhile 3DMCN-LFP/Fe-NSs cathode after cycles at 5 C, the D_{Li} value just reduced to 1.89×10^{-13} cm² s⁻¹ and Z_{Rct} value had no obvious change (Figure 5c and 5d), perhaps because of small changes in the very stable structure include 3DMCN and LiFePO₄ crystal.⁵⁵ In addition, 3DMCN-LFP/Fe-NSs sample has a higher σ value in low frequency, indicating lower Warburg impedance. In short, a low overall impedance so that the samples has a higher electron and Lithium-ion conductivity.

In order to verify the results of EIS, CV profiles of the commercial LFP and 3DMCN-LFP/Fe-NSs samples are shown in Figure 6, respectively. The curves showed obvious a pair of symmetrical oxidation (D_1) and reduction (R_1) peaks of peak voltage at 3.6 V and 3.3 V, corresponding to phase changes during the redox couple reaction (Fe^{2+}/Fe^{3+}) with the lithium-ion move in LiFePO₄ crystal structure. The CV test was well consistent with the charge-discharge curves shown in Figure 4a, and this means that the 3DMCN-LFP/Fe-NSs sample has a very stable structure.

The Randle-Sevcik formula (equation 1) was commonly used to estimate the lithium-ion diffusion coefficient of the charge-discharge platforms.⁵ The formula can be written as:

$$I_p = (2.69 \times 10^5) A n^{3/2} C_0 D^{1/2} \nu^{1/2} \quad (1)$$

Where I_p , A , n , C_0 , D , and ν correspond to the peak current, the surface area of the electrode, the number of electrons transferred in the electrode reaction, the concentration of Li⁺, the diffusion coefficient, the CV scanning rate, respectively.

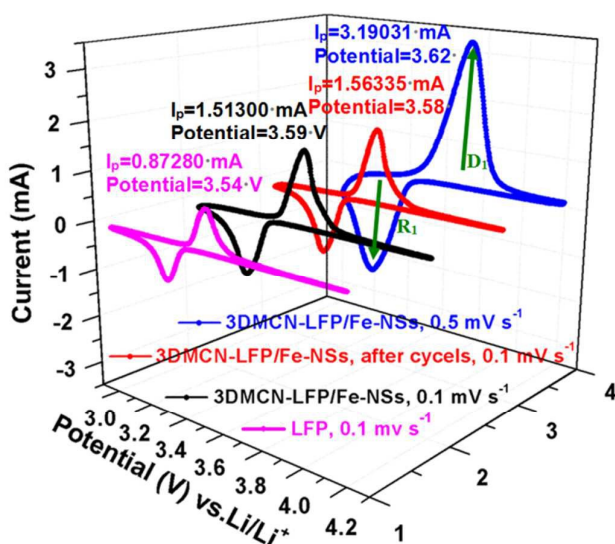


Figure 6 Cyclic voltammogram studies. CV curves of LFP and 3DMCN-LFP/Fe-NSs and the LFP/Fe sample after 50 cycles at 0.1 mV s^{-1} and the 3DMCN-LFP/Fe-NSs sample at 0.5 mV s^{-1} . I_p values in the figure correspond to the D_1 peak current.

CV method is considered to be a destructive characterization technique that it is not accurate to evaluate the diffusion coefficient of lithium-ion. For LiFePO_4 cathode, the D_{Li} value has positive correlations with the I_p^2/v . By a simple comparison of I_p^2 and v , the rough analysis of lithium-ion diffusion coefficient in cathode. The 3DMCN-LFP/Fe-NSs cathode has a higher D_{Li} value. After 50 cycles (from 0.1 C to 5C), the D_{Li} value of the 3DMCN-LFP/Fe-NSs cathode was slightly improved. This corresponding to EIS results. The result also found that lithium-ion diffusion coefficient is improving with the increase of the increase of scanning rate, but the electrochemical polarization serious. In conclusion, the 3DMCN-LFP/Fe-NSs sample has a lower Lithium-ion and electronic transport limitations, which is consistent with the good rate capability.

4. Conclusion

In conclusion, the $\text{LiFePO}_4/\text{Fe}$ nanospheres (LFP/Fe-NSs) coated with 3D mesoporous carbon network (3DMCN) have been synthesized by using a hydrophilic polysaccharides biomolecule—Alginate (ALG) as a nucleating agent, a structural biotemplate and a biocarbon source. The FePO_4 precursor nanoparticles encapsulated in algal gel by precipitating in situ for the first step, and then the 3DMCN-LFP/Fe-NSs nanocomposite was formed by using carbon thermal reduction method. The 3DMCN inherited ALG framework structure in the composite structure not only adheres the $\text{LiFePO}_4/\text{Fe}$ nanocrystallines, but also effectively reduces lithium-ion and electronic transport limitations and provides enough contact with the electrolyte. This unique porous structure can provide a large specific surface area for the electron delivery and buffer volume change of LiFePO_4 during lithium-ion insertion/desertion and crystal growth process. In the potential range of 2.0–4.2 V,

3DMCN-LFP/Fe-NSs cathode could deliver an initial discharge capacity of $177.3 \text{ mA h g}^{-1}$. After 70 cycles at varied current rates (from 0.1 C to 20 C), it still delivered a stable cycle performance, reversible capacity and high coulombic efficiency with high Lithium-ion diffusion coefficient. More importantly, this biomimetic method has simple process and abundant source, and may stimulate extensive research to fabricate other high-rate capability anodes and cathodes.

Acknowledgements

The authors thank the Natural Science Foundation of China (Grant no. 51172132, 51272144 and 51472127) for financial support. They also thank Shandong Provincial Key Laboratory of Processing and Testing Technology of Glass and Functional Ceramics for technological support. Prof. Yi Du and Xiwen Wang are thanked for technical support.

References

1. L. M. Guo, Y. L. Zhang, J. W. Wang, L. P. Ma, S. C. Ma, Y. T. Zhang, E. K. Wang, Y. J. Bi, D. Y. Wang, W. C. McKee, Y. Xu, J. T. Chen, Q. H. Zhang, C. W. Nan, L. Gu, P. G. Bruce and Z. Q. Peng, *Nat. Commun.*, 2015, **6**.
2. J. J. Wang and X. L. Sun, *Energy & Environmental Science*, 2015, **8**, 1110–1138.
3. K. Q. Ding, W. J. Li, Q. Wang, S. Y. Wei and Z. H. Guo, *J. Nanosci. Nanotechnol.*, 2012, **12**, 3813–3821.
4. Z. Y. Bi, X. D. Zhang, W. He, D. D. Min and W. Zhang, *RSC Advances*, 2013, **3**, 19744–19751.
5. I. D. Johnson, M. Lübke, O. Y. Wu, N. M. Makwana, G. J. Smales, H. U. Islam, R. Y. Dedigama, R. I. Gruar, C. J. Tighe, D. O. Scanlon, F. Corà, D. J. L. Brett and P. R. Shearing, *J. A. Darr, J. Power Sources*, 2016, **302**, 410–418.
6. X. D. Zhang, Z. Y. Bi, W. He, G. Yang, H. Liu and Y. Z. Yue, *Energy Environ. Sci.*, 2014, **7**, 2285–2294.
7. W. J. Zhu, H. Huang, W. K. Zhang, X. Y. Tao, Y. P. Gan, Y. Xia, H. Yang and X. Z. Guo, *Electrochim. Acta*, 2015, **152**, 286–293.
8. Y. Xia, Z. Xiao, X. Dou, H. Huang, X. H. Lu, R. J. Yan, Y. P. Gan, W. J. Zhu, J. P. Tu, W. K. Zhang and X. Y. Tao, *ACS Nano*, 2013, **7**, 7083–7092.
9. K. Q. Ding, W. J. Li, H. W. Yang, S. Y. Wei and Z. H. Guo, *J. New Mater. Electrochem. Syst.*, 2012, **15**, 63–69.
10. H. W. Wang, Z. J. Xu, H. Yi, H. G. Wei, Z. H. Guo and X. F. Wang, *Nano Energy*, 2014, **7**, 86–96.
11. C. X. Hu, S. M. Guo, G. X. Lu, Y. Fu, J. R. Liu, H. G. Wei, X. R. Yan, Y. R. Wang and Z. H. Guo, *Electrochim. Acta*, 2014, **148**, 118–126.
12. Y. L. Tan, K. Zhu, D. Li, F. Bai, Y. J. Wei and P. Zhang, *Chem. Eng. J.*, 2014, **258**, 93–100.
13. S. Z. Zhang, W. He, X. D. Zhang, G. H. Yang, J. Y. Ma, X. N. Yang and X. Song, *Electrochim. Acta*, 2015, **174**, 1175–1184.
14. J. Shin, M. Kim, J. Cirera, S. Chen, G. J. Halder, T. A. Yersak, F. Paesani, S. M. Cohen and Y. S. Meng, *J. Mater. Chem. A*, 2015, **3**, 4738–4744.
15. H. K. Kang, S. R. Lee, W. I. Cho and B. W. Cho, *Phys. Chem. Chem. Phys.*, 2013, **15**, 1569–1577.
16. X. Wang, K. Li, L. C. Jia, Q. Zhang, S. P. Jiang, B. Chi, J. Pu, L. Jian and D. Yan, *J. Power Sources*, 2015, **277**, 474.
17. C. Wu, H. Zhang, Y. X. Wu, Q. C. Zhuang, L. L. Tian and X. X. Zhang, *Electrochim. Acta*, 2014, **134**, 18–27.
18. J. Kim, M. K. Chung, H. K. Bok, J. H. Ku, S. Park, J. Ryu and S. M. Oh, *J. Electrochem. Soc.*, 2010, **157**, A412–A417.
19. L. X. Yuan, Z. H. Wang, W. X. Zhang, X. L. Hu, J. T. Chen, Y. H. Huang and J. B. Goodenough, *Energy Environ. Sci.*, 2011, **4**, 269–284.
20. H. L. Cao, X. Z. Wang, H. B. Gu, J. R. Liu, L. Q. Luan, W. Liu, Y. R. Wang and Z. H. Guo, *RSC Adv.*, 2015, **5**, 34566–34571.
21. S. M. Guo, J. R. Liu, S. Qiu, W. Liu, Y. R. Wang, N. N. Wu, J. Guo and Z. H. Guo, *J. Mater. Chem. A*, 2015, **3**, 23895–23904.
22. X. D. Zhang, Y. K. Hou, W. He, G. H. Yang, J. J. Cui, S. K. Liu, X. Song and Z. Huang, *Nanoscale*, 2015, **7**, 3356–3372.

23. X. Y. Tao, W. C. Chai, F. Q. Xu, J. M. Luo, H. Xiao, C. Liang, Y. P. Gan, H. Huang, Y. Xia and W. K. Zhang, *Electrochim. Acta*, 2015, **169**, 159-167.
24. L. H. Hu, F. Y. Wu, C. T. Lin, A.N. Khlobystov and L.J. Li, *Nat. Commun.*, 2013, **4**, 1687.
25. B. Qiu, Y. R. Wang, D. Z. Sun, Q. Wang, X. Zhang, B. L. Weeks, R. O'Connor, X. Huang, S. Wei and Z. Guo, *J. Mater. Chem. A*, 2015, **3**, 9817-9825.
26. J. Zhu, M. Chen, N. Yerra, N. Haldolaarachchige, S. Pallavkar, Z. Luo, T. C. Ho, J. Hopper, D. P. Young, S. Wei and Z. Guo, *Nanoscale*, 2013, **5**, 1825-1830.
27. X. Y. Tao, J. T. Zhang, Y. Xia, H. Huang, J. Du, H. Xiao, W. K. Zhang and Y. P. Gan, *J. Mater. Chem. A*, 2014, **2**, 2290-2296.
28. K. Q. Ding, H. B. Gu, C. B. Zheng, L. Liu, L. K. Liu, X. R. Yan and Z. H. Guo, *Electrochim. Acta*, 2014, **146**, 585-590.
29. S. M. Guo, J. R. Liu, S. Qiu, Y. R. Wang, X. R. Yan, N. N. Wu, S. Y. Wang and Z. H. Guo, *Electrochim. Acta*, 2016, **190**, 556-565.
30. S. M. Guo, G. X. Lu, S. Qiu, J. R. Liu, X. Z. Wang, C. Z. He, H. G. Wei, X. R. Yan and Z. H. Guo, *Nano Energy*, 2014, **9**, 41-49.
31. H. Gu, D. Ding, P. Sameer, J. Guo, N. Yerra, Y. Huang, Z. Luo, T. C. Ho, N. Haldolaarachchige, D. P. Young, A. Khasanov, Z. Guo and S. Wei, *ECS Solid State Lett.*, 2013, **2**, M65-M68.
32. X. D. Zhang, W. He, Y. Z. Yue, R. M. Wang, J. X. Shen, S. J. Liu, J. Y. Ma, M. Li and F. X. Xu, *J. Mater. Chem.*, 2012, **22**, 19948-19956.
33. X. Y. Du, W. He, X. D. Zhang, Y. Z. Yue, H. Liu, X. G. Zhang, D. D. Min, X. X. Ge and Y. Du, *J. Mater. Chem.*, 2012, **22**, 5960-5969.
34. J. Zhu, S. Pallavkar, M. Chen, N. Yerra, Z. Luo, H. A. Colorado, H. Lin, N. Haldolaarachchige, A. Khasanov, T. C. Ho, D. P. Young, S. Wei and Z. Guo, *Chem. Commun.*, 2013, **49**, 258-260.
35. Y. Xia, W. K. Zhang, Z. Xiao, H. Huang, H. J. Zeng, X. R. Chen, F. Chen, Y. P. Gan and X. Y. Tao, *J. Mater. Chem.*, 2012, **22**, 9209-9215.
36. A. Chojnacka, M. Molenda, M. Bakierska and R. Dziembaj, *ECS Transactions*, 2015, **64**, 165-171.
37. O. Catanzano, V. D' Esposito, S. Acierno, M. Ambrosio, C. De Caro, C. Avagliano, P. Russo, R. Russo, A. Miro and F. Ungaro, *Carbohydr. Polym.*, 2015, **131**, 407-414.
38. J. Rowbotham, P. Dyer, H. Greenwell, D. Selby and M. Theodorou, *Interface Focus*, 2013, **3**, 20120046.
39. M. H. Ryou, S. Hong, M. Winter, H. Lee and J. W. Choi, *J. Mater. Chem. A*, 2013, **1**, 15224-15229.
40. P. Singh, S. K. Singh, J. Bajpai, A. K. Bajpai and R. B. Shrivastava, *J. Mater. Res. Technol.*, 2014, **3**, 195-202.
41. J. Liu, Q. Zhang, Z. Y. Wu, J. H. Wu, J. T. Li, L. Huang and S. G. Sun, *Chem. Commun.*, 2014, **50**, 6386-6389.
42. W. He, X. D. Zhang, X. Y. Du, Y. Zhang, Y. Z. Yue, J. X. Shen and M. Li, *Electrochim. Acta*, 2013, **112**, 295-303.
43. Y. Habibi, L. A. Lucia and O. J. Rojas, *Chem. Rev.*, 2010, **110**, 3479-3500.
44. B. Wang, B. H. Xu, T. F. Liu, P. Liu, C. F. Guo, S. Wang, Q. M. Wang, Z. G. Xiong, D. L. Wang and X. S. Zhao, *Nanoscale*, 2014, **6**, 986-995.
45. X. L. Fan, J. L. Luo, C. Shao, X. S. Zhou and Z. J. Niu, *Electrochim. Acta*, 2015, **158**, 342-347.
46. J. Q. Zhou, T. Qian, T. Z. Yang, M. F. Wang, J. Guo and C. L. Yan, *J. Mater. Chem. A*, 2015, **3**, 15008-15014.
47. J. Liu, T. E. Conry, X. Song, M. M. Doeff and T. J. Richardson, *Energy Environ. Sci.*, 2011, **4**, 885-888.
48. R. G. Mei, Y. F. Yang, X. R. Song, Z. G. An and J. J. Zhang, *Electrochim. Acta*, 2015, **153**, 523-530.
49. G. Q. Tan, F. Wu, L. Li, R. J. Chen and S. Chen, *J. Phys. Chem. C*, 2013, **117**, 6013-6021.
50. G. L. Wang, Z. P. Ma, G. J. Shao, L. X. Kong and W. M. Gao, *J. Power Sources*, 2015, **291**, 209-214.
51. J. F. Qian, W. A. Henderson, W. Xu, P. Bhattacharya, M. Engelhard, O. Borodin and J.G. Zhang, *Nat Commun*, 2015, **6**.
52. N. Balke, S. Jesse, A. Morozovska, E. Eliseev, D. Chung, Y. Kim, L. Adamczyk, R. Garcia, N. Dudney and S. Kalinin, *Nat. Nanotechnol.*, 2010, **5**, 749-754.
53. S. Y. Gao, Y. F. Su, L. Y. Bao, N. Li, L. Chen, Y. Zheng, J. Tian, J. Li, S. Chen and F. Wu, *J. Power Sources*, 2015, **298**, 292-298.
54. X. D. Zhang, X. L. Xu, W. He, G. H. Yang, J. X. Shen, J. H. Liu and Q. Z. Liu, *J. Mater. Chem. A*, 2015, **3**, 22247-22257.
55. J. H. Kim, S. C. Woo, M. S. Park, K. J. Kim, T. Yim, J. S. Kim and Y. J. Kim, *J. Power Sources*, 2013, **229**, 190-197.

110

Graphical abstract

three-dimensional mesoporous carbon network-coated $\text{LiFePO}_4/\text{Fe}$ nanospheres with high-rate capability.

